

THE ABUNDANCE OF LOW-LUMINOSITY LYMAN α EMITTERS AT HIGH REDSHIFT¹

MICHAEL R. SANTOS², RICHARD S. ELLIS, JEAN-PAUL KNEIB³
 California Institute of Technology and
 105-24 Caltech, Pasadena, CA 91125

JOHAN RICHARD
 Observatoire de Midi-Pyrénées and
 UMR5572, 14 Av. Edouard Belin, F-31400 Toulouse, France

AND
 KONRAD KUIJKEN
 Sterrewacht Leiden and
 P.O. Box 9513, NL-2300 RA, Leiden, The Netherlands

ABSTRACT

We derive the luminosity function of high-redshift Lyman α emitting sources from a deep, blind, spectroscopic survey that utilized strong-lensing magnification by intermediate-redshift clusters of galaxies. We observed carefully selected regions near 9 clusters, consistent with magnification factors generally greater than 10 for the redshift range $4.5 < z < 6.7$. Eleven emission-line candidates were located in the range $2.2 < z < 5.6$ whose identification we justify as Lyman α , in most cases via further spectroscopic observations. The selection function we constructed for our survey takes into account our varying intrinsic Lyman α line sensitivity as a function of wavelength and sky position. By virtue of the strong magnification factor, we provide constraints on the Lyman α luminosity function to unprecedented limits of 10^{40} erg s⁻¹, corresponding to a star-formation rate of $0.01 M_{\odot}$ yr⁻¹. Our cumulative $z \simeq 5$ Lyman α luminosity function is consistent with a power law form, $n(> L) \propto L^{-1}$ over 10^{41} to $10^{42.5}$ erg s⁻¹. When combined with the results of other surveys, limited at higher luminosities, our results suggest evidence for the suppression of star formation in low-mass halos, as predicted in popular models of galaxy formation.

Subject headings: galaxies: formation, evolution, high-redshift, luminosity function—cosmology: observations—gravitational lensing

1. INTRODUCTION

The epoch of cosmic reionization, when the intergalactic hydrogen in the universe transitioned from neutral to ionized, is the current frontier of observational cosmology. QSOs discovered by the Sloan Digital Sky Survey (SDSS) indicate that reionization was just finishing at $z \simeq 6$ (Becker et al. 2001; Djorgovski et al. 2001; Fan et al. 2002). Recent results from the *WMAP* satellite suggest that significant reionization of the universe took place by $z \sim 12$ (Spergel et al. 2003). The sources that reionized the universe, however, are still unknown: at $z \sim 6$ neither bright QSOs discovered by SDSS (Fan et al. 2001) nor faint AGN from deep x-ray observations (Barger et al. 2003) produced enough photons to reionize the universe. Other evidence from the temperature and ionization state of the intergalactic medium (IGM) suggests that, though QSOs dominated the metagalactic ionizing background at $z \sim 3$, the spectrum was softer at reionization (e.g. Sokasian, Abel, & Hernquist

2003). Accordingly, hot stars in early star-forming systems may have been the dominant source of reionizing photons. One goal of the forthcoming NASA/ESA *James Webb Space Telescope (JWST)*, a 6-meter IR telescope scheduled for launch in 2010, is to study the formation of the first generations of galaxies and their contribution to reionization (Mather & Stockman 2000).

Early galaxies played many important roles beyond their involvement with reionization. The IGM was enriched well above the primordial metal abundance by $z = 5$ (Songaila 2001; Pettini et al. 2003); additional evidence for early metal production comes from metal-poor globular clusters in the Milky Way. Age estimates imply a formation epoch of $z \gtrsim 4$ for current cosmological parameters (Krauss & Chaboyer 2003), but the typical metallicity of these objects is 10^{-2} of the solar value (Harris 1996). The stars responsible for reionization and early metal production may still be present in some form today. It is an important challenge to identify the transition between the very first, metal-free, stars, and Population II stars, because of the strong constraints on the metallicity of low-mass stars provided by studies of halo stars in the Milky Way. A complete understanding of the metallicity distribution of old Galactic stars will benefit from direct observation of very high redshift star formation in *proto-galactic systems that will evolve into galaxies like the Milky Way*.

In advance of *JWST*, which will use IR capabilities to observe galaxies before the end of reionization in rest-

Electronic address: mrs@tapir.caltech.edu

¹ Data presented herein were obtained at the W.M. Keck Observatory, which is operated as a scientific partnership among the California Institute of Technology, the University of California and the National Aeronautics and Space Administration. The Observatory was made possible by the generous financial support of the W.M. Keck Foundation.

² current address Institute of Astronomy, University of Cambridge, Madingley Road, Cambridge CB1 1BL, U.K.

³ also Observatoire de Midi-Pyrénées, UMR5572, 14 Av. Edouard Belin, F-31400 Toulouse, France

frame UV and optical light, current ground-based facilities have the opportunity to discover and characterize star-forming galaxies near the epoch of reionization with rest-frame UV observations. In particular, the identification of Lyman α emission from star-forming regions of early galaxies has proven to be a powerful tool for discovering $z > 4$ galaxies and measuring their redshifts (see Section 2). The redshift range $5 < z < 7$ is of particular interest for two reasons. One is that the very detection of Lyman α emission may place a constraint on the progress of reionization (Rhoads & Malhotra 2001; Haiman 2002; Hu et al. 2002a; Rhoads et al. 2003): it is difficult to observe Lyman α emission from galaxies embedded in a neutral IGM, but the strength of the constraint derived from the successful detection of Lyman α depends on the assumed properties of the sources (Santos 2003). The second important reason to study galaxy formation during and after reionization is that an intense UV background and 10^4 K IGM is predicted to suppress star-formation in galaxies that form after reionization (Barkana & Loeb 1999; Gnedin 2000; Benson et al. 2002a). There is a discrepancy between some theoretical predictions of the abundance of dark matter halos on dwarf-galaxy mass scales and the number of observed dwarf satellites in the Local Group (Moore et al. 1999). Reionization may sterilize many dwarf galaxy-scale halos to star formation, so that the luminous satellites of the Milky Way are dwarf galaxies formed before reionization, and the remaining satellite halos are empty of stars and thus dark (Benson et al. 2002b; Somerville 2002).

This paper presents the results of a spectroscopic Lyman α emission-line survey for galaxies at $2.2 < z < 6.7$ that utilizes the strong-lensing properties of intermediate-redshift clusters to magnify the surveyed regions. In Section 2 we review the use of Lyman α surveys as probes of early star formation. Section 3 motivates the importance of surveys for low-luminosity galaxies. Section 4 describes the advantages of a survey utilizing strong lensing and details our survey strategy, targets, observations, and data reduction. In Section 5 our Lyman α emission-line detections are presented. We compute our survey volume and source number density in Section 6. Section 7 compares the results of our survey to other surveys and theoretical models. In Section 8 we summarize.

Throughout this paper we use a Λ CDM cosmological model with $(\Omega_m, \Omega_\Lambda, \Omega_b, \sigma_8) = (0.3, 0.7, 0.043, 0.9)$ and $h \equiv H_0/(100 \text{ km s}^{-1} \text{ Mpc}^{-1}) = 0.7$; these values are consistent with the values derived in Spergel et al. (2003).

2. LYMAN α SURVEYS

The primary appeal of Lyman α emission as a signpost to high-redshift galaxy formation is that it traces star formation at a wavelength that conveniently redshifts into the visible and near-IR, where sensitive, high-angular resolution observations are currently most practical. The Lyman α emission line may be quite strong, but its luminosity is quite sensitive to physical details of the nature and geometry of the star-forming regions. Because Lyman α emission traces hydrogen recombinations, it is intimately related to the production of ionizing photons by the stars present. Both the initial mass function (IMF) and metallicity of the stars affect their production rate of ionizing photons. However, if the IMF and metal-

licity are constrained to reasonable ranges, the ionizing photon production rate can be reliably connected to the star-formation rate.

The major complication for the interpretation of Lyman α line strengths is the effect of the nebula around the star-forming region. Hydrogen at low density does not recombine quickly, so, e.g., ionizing photons that escape into the IGM are “lost” for the purposes of producing a Lyman α emission line. Even after a hydrogen recombination produces a Lyman α photon, which happens for about two thirds of the recombinations (Osterbrock 1989), there are many ways in which the photon may be destroyed prior to escape. The resonant nature of the Lyman α transition results in a very short mean free path, even in a mostly ionized nebula. Consequently, if dust is mixed in with the gas, then the chance of absorption by a dust grain may be higher for a Lyman α photon than a non-resonantly scattered photon at the same wavelength (but see Neufeld 1991, for an alternative). The dust content of very high-redshift galaxies is still relatively unconstrained, and will likely remain so at least until *JWST*.

On the positive side, Lyman α is the intrinsically strongest recombination line from an H II region. Another meritorious aspect of Lyman α is that its emission strength does not strongly depend on the metallicity of the ionized gas (the only effect is from the temperature of the photoionized gas, which depends on metallicity); consequently, it can be used as a tracer for truly primordial star formation, where dust extinction is also believed not to be a problem.

Partridge & Peebles (1967) introduced a model of galaxy formation “to assess the general possibility of observing distant, newly formed, galaxies.” In their model they estimated that 6–7% of the luminosity of early galaxies would be emitted in the Lyman α emission line: they predicted line luminosities of $2 \times 10^{45} \text{ erg s}^{-1}$ over galaxy formation time-scales of $3 \times 10^7 \text{ yr}$. The predictions of Partridge & Peebles (1967) and others led to many observational surveys for Lyman α emission from high-redshift galaxies, reviewed by Pritchett (1994, §4.5). Pritchett summarized the status of searches at that time with “no emission line primeval galaxies have been found” despite 16 cited surveys covering various redshifts ranges from $z = 2$ to $z = 5$. In striking contrast to these pioneering explorations, many high-redshift Lyman α emission-line galaxies have been discovered and confirmed in the past 8 years. Stern & Spinrad (1999, §4) and Taniguchi et al. (2003) have reviewed recent progress, and we provide a brief summary here.

The search technique that has dominated recent success in the discovery of large numbers of Lyman α emission-line galaxies at $z > 4$ is narrow-band photometry. This approach uses a narrow ($\sim 100 \text{ \AA}$) filter chosen to lie in a spectral region of low sky background; such surveys cover relatively large areas of sky with sensitivity to Lyman α emission over a small window in redshift, $\Delta z \sim 0.1$. Many groups have now performed successful blind narrow-band surveys for $z > 4$ galaxies: Hu, Cowie, & McMahon (1998) and Rhoads et al. (2000) at $z = 4.5$; Ouchi et al. (2003) at $z = 4.9$; Hu, McMahon, & Cowie (1999), Rhoads & Malhotra (2001), and Rhoads et al. (2003) at $z = 5.7$; and Hu et al. (2002a) and Kodaira et al. (2003)

at $z = 6.5$.

Spectroscopic surveys provide a complementary technique to the narrow-band method. For equal observing time at one position, spectroscopic searches at optical wavelengths can cover a large range in redshift, $\Delta z \sim 3$, to better line flux sensitivity than a corresponding narrow-band survey. However, the area surveyed by a long slit is typically $\sim 5 \times 10^{-2}$ arcmin², in contrast to 20–2000 arcmin² for an imaging camera. Deep long slit observations of other targets have been searched for serendipitous detection of high-redshift galaxies. These techniques discovered the first confirmed $z > 5$ galaxy (Dey et al. 1998) and subsequently turned up a few more $z > 4$ sources (Hu et al. 1998; Weymann et al. 1998). Serendipitous surveys will likely continue to play a role in discovering high-redshift galaxies, since the deepest spectra on the largest telescopes are likely to be pointed observations rather than devoted emission-line surveys.

Under sky-limited conditions, it is simple to show that the signal-to-noise ratio \mathcal{R} that is reached on pure emission-line sources of flux F in a survey over sky area A and wavelength range Λ , with area and wavelength coverage ΔA and $\Delta \lambda$, seeing disk δA and spectral resolution $\delta \lambda$, is given by

$$\mathcal{R} = \frac{Ft}{\sqrt{S\delta A\delta \lambda t}} = \frac{F\sqrt{T/(A\Lambda)}}{\sqrt{S\frac{\delta A}{\Delta A}\frac{\delta \lambda}{\Delta \lambda}}}, \quad (1)$$

where t and T are the lengths of individual exposures, and of the whole survey, respectively, and S is the sky surface brightness per unit wavelength. The tradeoff is thus between the number of seeing elements that can be observed simultaneously ($O(N^2)$ in case of an imaging survey, $O(N)$ for a long-slit spectral survey) vs. the number of spectral elements (1 for a narrow-band survey, $O(N)$ for a spectral survey). As each is limited by detector sizes, both modes can in principle offer comparable survey speed to a given flux limit (the argument applies also to surveys with integral field unit spectrographs). Spectral surveys are advantageous for targeting small regions of the sky and covering a large wavelength range, or for simply going as deep as possible in a given amount of time; narrow-band surveys are optimal in the opposite regime of wide area, small wavelength range. A further advantage of high-spectral resolution surveys is that the night sky emission lines can be maximally avoided, which is not possible with the typical bandwidths employed in narrow-band surveys.

A few other hybrid techniques combine aspects of the narrow-band imaging and long-slit spectroscopy approaches. Maier et al. (2003) used an imaging Fabry-Perot interferometer to take sequences of narrow band images within the night-sky windows corresponding to $z = 4.8, 5.7, 6.5$, and have confirmed discoveries at $z = 4.8$ and 5.7 . Recently Lilly et al. (2003) and Martin & Sawicki (2003) used a “slit-let” slit mask with a narrow-band filter to do spectroscopic surveys over a relatively large areas and narrow redshift windows. There is also an ongoing *HST* program to use slitless spectroscopy with the ACS camera grism to discover high-redshift Lyman α emission (J. E. Rhoads, priv. comm.).

3. SEARCHES FOR DISTANT LOW-LUMINOSITY GALAXIES

In this section we present the motivation for conducting a survey devoted specifically to low-luminosity $z \sim 5$ Lyman α emitting galaxies ($\lesssim 10^{42}$ erg s⁻¹ in the Lyman α line), an unexplored region of survey parameter space.

At $z \sim 5$, the luminous Lyman α galaxies (§2) and QSOs (e.g., Fan et al. 1999, 2000, 2001) discovered so far represent the rarest and most spectacular tail of the range of structure formation scales (e.g., Barkana & Loeb 2003 suggested that the high- z SDSS QSOs reside in $10^{12} M_{\odot}$ virialized halos). They almost certainly evolve into the rarest and most massive environments in the local universe: rich clusters of galaxies. In striking contrast, the characteristic mass of virialized halos at $z \sim 5$ is only $10^9 M_{\odot}$; if such an object steadily converts its $\sim 10^8 M_{\odot}$ of baryons into stars, it will have a star-formation rate of only $\sim 0.1 M_{\odot} \text{ yr}^{-1}$.

These objects, which we will refer to as low-mass halos, would not be detectable in any of the surveys cited above, but our understanding of galaxy formation depends crucially on constraining their properties for three important reasons: First, they represent the most common environment *by mass* of virialized halos (the peak of the mass-weighted mass function is always near the characteristic mass); consequently, if low-mass halos form stars efficiently, they could dominate the star-formation rate at high redshift. Second, they are the progenitors of common galaxies in poor environments, like the Milky Way, under the current paradigm of structure formation. The detection of low-mass sources is a direct test of the “bottom-up” description of galaxy assembly. Third, low-mass objects have a unique link to the IGM: kinetic energy injected into the IGM by photoionization at $z \gtrsim 6$ is expected to raise the cosmic Jeans mass and inhibit gas cooling; this effect has no consequence for the brightest sources residing in deep potential wells, but may heavily suppress star formation in $10^9 M_{\odot}$ objects (e.g., Barkana & Loeb 1999; Gnedin 2000). This Jeans-mass effect has been cited as the solution for the Cold Dark Matter “crisis” of over-predicting the number of Milky Way satellite galaxies compared to observation (Benson et al. 2002b; Somerville 2002). Low-mass halos also place relevant constraints on the energy scale of dark matter in Warm Dark Matter models (Z. Haiman, priv. comm.).

A practical and strategic advantage in characterizing the luminosity function at low luminosities is to determine the optimum survey depth for future surveys that aim to discover large numbers of $4 \lesssim z \lesssim 7$ galaxies. If the luminosity function were very steep, then deep surveys such as ours would be more efficient than shallower, wider field surveys. Theoretical prejudice suggests that the luminosity function should have a steep effective slope in the region associated with the exponential cut-off of the number density of underlying halos, assuming some sort of mass-to-luminosity correspondence. Previous non-detections combined with recent successes seem to bear this out (Pritchet 1994, and see below). That is, current surveys may be approaching the characteristic luminosity; however, the characteristic luminosity and luminosity function shape have yet to be well constrained. In the local universe, luminosity functions based on star-formation rate estimators such as H α luminosity roughly follow the Schechter function (Schechter 1976) form of

power-law behavior at low luminosity, reflecting the underlying power-law of the mass function, albeit with possibly a different slope (e.g., Gallego et al. 1995).

The predicted suppression of star formation in halos with small potential wells suggests that the Lyman α luminosity function at $z \sim 5$ may have a modified shape. The reason is that the characteristic mass scale where the exponential tail and power law regions of the mass scale meet, $\sim 10^9 M_\odot$, corresponds quite closely to the mass scale where a number of physical mechanisms may suppress star formation. We described the effect of a hot IGM above. In addition, energy injected in the ISM of star-forming galaxies by stellar winds and supernovae (called “negative feedback,” or just “feedback”) is predicted to heavily suppress star formation in halos with circular velocities below about 100 km s^{-1} (Dekel & Silk 1986), corresponding to a mass scale at $z \sim 5$ of $\sim 10^{11} M_\odot$. A current implementation of feedback by Benson et al. (2002a) shows the importance of feedback on the high-redshift star-formation rate. This effect complements the inhibiting effects of a hot IGM on star formation in low-mass halos. A third mechanism that may reduce star formation preferentially in low-mass halos is the effect of large-scale winds blown by star-forming galaxies. Scannapieco, Ferrara, & Broadhurst (2000) and Scannapieco & Broadhurst (2001) computed the influence of winds blown out through the IGM by the first galaxies to form. They concluded that these winds effectively sweep gas out of nearby halos in the process of collapsing, meaning that even though the dark matter continues its collapse to virialization, there is little corresponding star formation because of the lack of baryons. In their model winds influence the entire star-formation history of the universe, but at $z \sim 5$ particularly suppress star-formation in halos smaller than $\sim 10^{10} M_\odot$.

Figure 1 is a schematic illustration of the possible effect of the suppression of star formation in low-mass halos. The solid curve is the mass function of halos at $z = 5$ (Sheth & Tormen 2002), and we have converted the mass scale on the top axis into a star-formation rate on the bottom axis using a simple prescription (see Section 7.2). In this simple model, the Lyman α line luminosity function, if interpreted as directly proportional to that of the SFR, would have the shape of the solid curve. We have introduced the suppression of star formation in low mass halos by using the prescription of Gnedin (2000) to efficiently filter out gas from halos below a critical mass scale M_F , the filtering mass (Gnedin 2000). Each of the broken curves is the shape of the Lyman α line luminosity function we expect (again assuming it scales with SFR) after applying filtering on a different mass scale. Ultimately the filtering mass, and thus the physics described in the previous paragraph, may be constrained directly by a measurement of the shape of the star-formation rate function, along with estimates of the corresponding halo masses (see Section 7.2).

Only recently have deep observations with large telescopes even detected $z \sim 5$ Lyman α emitting galaxies; the detailed form of the luminosity function will not be well-constrained in the immediate future. However, our low-luminosity Lyman α survey, and others like it, in concert with surveys at higher luminosities, may constrain or detect the break in the luminosity function associated with the characteristic halo mass and where star forma-

tion is suppressed.

4. OBSERVATIONS

4.1. Survey Strategy

The goal of our survey is to extend the census of Lyman α sources at $z \sim 5$ to the faintest luminosities possible with existing observational facilities. We achieved this through deep spectroscopic exposures on areas of sky strongly magnified by gravitational lensing.

Strong gravitational lensing by rich clusters of galaxies at $z \sim 0.2$ is an invaluable resource to a survey covering a very small area of sky to great depth, as such clusters magnify background high-redshift sources by greater than a factor of 10 over regions of roughly 0.1 arcmin^2 in the image plane. This advantage comes at a price: lensing increases the apparent area of a background source at fixed surface brightness, so that the pointing is deeper by a factor of the magnification, \mathcal{M} , but covers only $1/\mathcal{M}$ of the area of an equivalent unlensed pointing (assuming unresolved sources). This is a superior strategy for a deep, narrow survey. Achieving the same depth and area in an unlensed survey would require a factor of \mathcal{M} more observing time, a huge difference for $\mathcal{M} \sim 10$.

Only a small area of the whole sky, $\sim 100 \text{ arcmin}^2$, is magnified by a factor of 10 or more by clusters; this sets a fundamental limit to the areal coverage of any survey utilizing strong lensing by clusters. For a large survey that detected many sources, statistical information about the distribution of magnification over the survey area might be sufficient to construct a Lyman α emitter luminosity function. However, since we planned to survey a small area and detect only a few sources, we chose to observe clusters with *HST* imaging and spectroscopic redshifts for many of the identified arcs and multiple images (e.g., Kneib et al. 1996). These are currently available for only a small fraction of strong-lensing clusters. The positions and spectroscopic redshifts of the arcs constrain the distribution of mass in the cluster which can, in turn, be used to predict a magnification map of the cluster for high-redshift sources. Since lensing depends on the angular-diameter distance between the source and the lens, and that distance changes slowly with redshift at $z \sim 5$, the sky area with large magnification is fairly independent of the source redshift for $z > 3$.

Given that high-quality lens models are only available for about a dozen clusters observable from Hawaii, the total area available to us for a survey is currently quite small. To make the most of this limited resource, we conducted a spectroscopic survey. The advantage of a spectroscopic survey is that Lyman α emission can be simultaneously surveyed for over a redshift range $2.2 < z < 6.7$. The primary draw-back of a spectroscopic survey was that, with the instrumentation available, the most efficient technique was slit spectroscopy. The geometry of a long slit is not well matched to the lensed region of sky (see Fig. 2), thus some of the slit area covers area outside the cluster that is not strongly magnified.

A long-slit survey does have other advantages. We can expect many emission-line sources in our survey other than Lyman α ; in particular, optical lines associated with strong star formation, such as [O II] 3726, 3729 Å; H β 4861 Å; [O III] 4959, 5007 Å; and H α 6563 Å. Low-resolution spectroscopy with large wavelength coverage

allows the rejection of many potential low-redshift contaminants through the identification of other emission lines. However, the [O II] doublet can be difficult to resolve at low dispersion and, if redshifted to $z \sim 1$, there are often no other strong emission lines present in the optical spectrum. Thus final identification of an emission line as Lyman α may require follow-up spectroscopy at intermediate resolution.

Redshift identification is aided by two additional factors. Deep optical broadband imaging, available in at least one band for well-studied clusters, can be used, as in narrow-band searches, as a rejection filter: if a putative Lyman α system shows much observable flux shortward of Lyman α , then it is not likely a correct line identification, because the intrinsic UV spectrum combined with IGM absorption create a strong decrement across the Lyman α emission line (e.g., Songaila & Cowie 2002). The second tool is available when two or more images (due to strong lensing) of the same high-redshift source are discovered. In this case the lensing model itself may place a reasonably strong constraint on the redshift of the system based on the observed image positions and flux ratios (Kneib et al. 1996).

The deepest survey for a given observing time would be to devote all of the time to a single slit position. However, we expect Lyman α sources to be clustered, resulting in a non-Poisson distribution. To estimate an accurate luminosity function we surveyed several independent volumes (via surveying behind several lensing clusters) to ameliorate cosmic variance and recover the Poisson noise limit (see Section 7.2).

4.2. Survey Parameters

Table 1 summarizes the 9 lensing clusters of our survey. We have constructed a detailed mass model for each, based on *HST* imaging and lensed arc redshifts.

Details of our spectroscopic observations are listed in Table 2. Clusters that were observed at multiple position angles are designated further by an identification number. We used the double-beam Low Resolution Imaging Spectrograph (LRIS, Oke et al. 1995) in long-slit mode on the Keck I 10-meter telescope at Mauna Kea to perform our survey. For the 2000 March observations we used a slit $0.7''$ wide and a spectroscopic range of $\lambda\lambda$ 6800–9500 Å (corresponding to Lyman α with $4.6 < z < 6.8$), using a 600-line grating blazed at λ 7500 Å which gave a resolution of $\simeq 3.0$ Å. In 2001 April we switched to a $1.0''$ -wide slit and used a 600-line grating blazed at $1 \mu\text{m}$ over the same wavelength range as above, at a resolution of $\simeq 4.0$ Å. Starting in 2001 April we also began using a 300 line grism blazed at 5000 Å and a dichroic at 6800 Å to simultaneously take spectra on the blue arm of the spectrograph, over $\lambda\lambda$ 4000–6700 Å (corresponding to Lyman α from $2.2 < z < 4.5$) at 3.5 – 4 Å resolution.

The length of the spectrographic slit was $175''$. We mapped an area on the sky via offsetting the telescope perpendicular to the long axis of the slit by a distance equal to the slit width. At each slit position we made two exposures of 1000 sec to facilitate cosmic ray rejection. Each map comprised 5–10 adjacent slit positions at the same position angle, giving contiguous survey areas on the sky of 875–1750 arcsec².

The pointing of the slit on the sky was verified by reg-

istration of images from the LRIS slit-viewing guide camera to the *HST* images of the cluster (because the clusters are rich in bright galaxies, there were always many sources in the slit-viewing guide camera images). Our sequence of slit offsets typically agreed with a regular spacing of the slit width to a precision of $0.1''$ (10% of the $1''$ slit). More importantly, registration of the slit position on the *HST* image enabled us to look for a broadband counterpart at the location of emission lines detected in our spectra.

The areas mapped by the procedure above were chosen to take advantage of the strong magnification of background sources provided by the foreground cluster. The magnification map of the sky around the cluster is constrained by the distribution of visible light in the cluster and the measured velocity dispersion of some cluster members, but is crucially verified and refined by including information from the locations and redshifts of strongly lensed sources. These background galaxies, generally brighter and at lower redshift than the $z > 4.5$ sources we searched for, have been the target of previous observations (e.g., Kneib et al. 1996).

We used up-to-date cluster mass models to generate redshift-dependent maps of the magnification toward $4 < z < 7$ sources using the LENSTOOL software developed by Kneib (1993). The angular diameter distance between the cluster and those redshifts depends only weakly on redshift, so we were able to choose areas on the sky with high magnification over our entire redshift range of interest.

The geometry of the magnification map is generally characterized by two concentric ring-like curves of formally infinite magnification, called the inner and outer critical lines. These are related to the location in the image plane of the caustic of an elliptical potential (Blandford & Narayan 1992), but modified by the deviations of the projected lensing potential from an ellipse. The areas of highest magnification are found next to the critical curves, so our survey maps generally follow the outer critical line. The outer critical line is more amenable to long-slit mapping because of its greater length on the sky and its less curved form. However, in one case (Abell 1689) we mapped sky near the inner critical line as well. Lensed sources close to the critical line are often multiply imaged, forming a merging pair on either side of the critical line. We considered this when we chose our map locations, but the irregular shape of the critical line, compared to the straight shape of our slit, limited the extent to which we could map exclusively one side of the critical line.

Figure 2 summarizes the adopted strategy for each cluster in the context of the location of the critical line for a lensed source at $z = 5$ (dotted lines). In the most massive clusters with the best mass models, such as Abell 1689 and Abell 2218, we made multiple maps (see also Table 2). In these cases each survey region is labeled by a number corresponding to the observations listed in Table 2.

The total area on the sky covered by our survey was 4.2 arcmin^2 . The effective areal coverage of the survey is smaller due to lensing by a spatially variable magnification factor (see Section 6.1.1).

4.3. Candidate Selection and Catalog

The 2-D spectroscopic data were reduced using standard techniques in the NOAO/IRAF software environment⁴. Cosmic rays were rejected from each pair of images at a given location with the L.A.COSMIC routine (van Dokkum 2001) and sky emission was removed by subtracting block-filtered data. Sky subtraction was not photon-limited on the strong night sky lines due to the presence of fringing features; we account for this when determining our sensitivity in Section 6. We calibrated our absolute efficiency with observations of spectrophotometric stars (Massey & Gronwall 1990).

The sky-subtracted 2-D spectral images were independently inspected by two of the authors (RSE and JR) and a catalog of 46 candidate Lyman α emission lines was compiled. Astrometric positions were determined for each and the *HST* images inspected for sources at the relevant location. In some cases, candidates were located beyond the boundary of the *HST* images and ground-based images were used.

Candidate Lyman α emission lines were characterized on the basis of several criteria. First, the full spectrum (generally 4000–9500 Å) was closely examined for other emission lines. On a second pass, candidates were ranked as marginal or promising depending on their apparent strength and spatial extent. Out of the initial list of 46, 7 sources are confirmed Lyman α lines at $2.8 < z < 5.7$, and 4 sources are promising candidates that we identify as likely to be Lyman α lines. Those 11 sources are listed in Table 3, with observed line fluxes for detections at $z > 4.5$ (on the red arm of the spectrograph).

4.4. Intermediate-resolution Spectroscopy

The [O II] 3727 Å doublet has a rest-frame separation of 3 Å. Thus at $z \sim 1$, when the doublet is redshifted into our most important spectral range, the observed doublet separation is ~ 6 Å. This is close to our LRIS spectral resolution of 4 Å, so to determine whether any of our Lyman α line candidates were unresolved [O II] doublets, we followed up 15 candidates with the Echellette Spectrograph and Imager (ESI, Sheinis et al. 2002). We took spectra using the echelle mode and a 0.75" slit, which delivered a spectral resolution of $R = 6000$. The exposure times varied depending on candidate strength. ESI spectroscopy confirmed three candidates as Lyman α emission lines (see Table 3), at $z = 3.27$, $z = 3.62$, and the $z = 5.57$ galaxy presented in Ellis et al. (2001). Additionally, several of the original candidates turned out to be [O II] 3727 Å at $z \simeq 1$.

5. DETECTIONS

5.1. $z > 4.5$

We detected three convincing Lyman α sources with $z > 4.5$ (see Table. 3); each was detected in photometric conditions. Figure 3 shows their two-dimensional spectra, and Fig. 4 shows a magnified view of the Lyman α emission line as well as *HST* images of the source locations.

We discovered a source toward Abell 2218 at $z = 5.6$ that we discussed in detail in Ellis et al. (2001). That

source is strongly magnified (a factor of 33) and multiply imaged: we used the *HST* data to locate a second image outside of our survey region. The redshift identification was confirmed by an intermediate-resolution spectrum of both images, showing them to be identical, with P-Cygni line profiles characteristic of Lyman α , and certainly not the [O II] 3727 Å doublet. Our lensing model additionally constrained the redshift of the source to be consistent only with the identification of the line as Lyman α . The unlensed luminosity in the Lyman α line is $(7.8 \pm 0.8) \times 10^{41}$ erg s⁻¹.

We blindly recovered a $z = 4.89$ galaxy in Abell 1689 that was discovered originally by Frye, Broadhurst, & Benítez (2002). This object is multiply imaged, and the Frye et al. (2002) spectrum shows a strong break across the line and metal absorption lines in the continuum redward of Lyman α , confirming the redshift. We estimate the magnification of this source at a factor of 7.2, within the range of 3–14 suggested by the coarser modeling of Frye et al. (2002). The unlensed luminosity in the Lyman α line is $(7.4 \pm 0.7) \times 10^{42}$ erg s⁻¹.

In the field of Cl1358, we discovered a source at $z = 4.92$, the same redshift as that of the strongly lensed arc discovered by Franx et al. (1997). We believe our source is likely associated, as an additional component, with that responsible for the giant arc. The magnification is $\times 10$, giving an unlensed luminosity in the Lyman α line of $(2.5 \pm 0.3) \times 10^{42}$ erg s⁻¹.

In addition to these confirmed sources, we discovered two more sources that we consider likely to be Lyman α emission lines at $z > 4.5$ (see Table. 3). We discovered a source in the field of Abell 773 that we consider to be a good candidate for Lyman α emission at $z = 4.74$. If this is the correct identification, the unlensed luminosity in the Lyman α line is $(2.8 \pm 0.6) \times 10^{41}$ erg s⁻¹, using a magnification factor of 9.5. The other likely source was discovered in non-photometric observations; though we lack absolute flux calibration for this source, we applied a systematic photometric correction that we consider uncertain up to a factor of approximately 2. The likely $z = 4.77$ source is in the field of Abell 963, magnified by 2.2 times. The source would then have an unlensed Lyman α line luminosity of $(1.4 \pm 0.2) \times 10^{42}$ erg s⁻¹ (statistical error only). Two-dimensional spectra of the emission lines and images of the likely candidates are provided in Fig. 5.

5.2. $z < 4.5$

We detected with certainty four Lyman α emission-line sources at $z < 4.5$. One was a blind recovery of a $z = 2.80$ source behind Abell 370 discovered by Ivison et al. (2002), and a second is another galaxy also at $z = 2.80$ in the same field. Two are new detections, at $z = 3.27$ and $z = 3.62$, both behind Abell 963. Two more good candidate Lyman α emission-line source identifications are pending. In addition two galaxies behind Abell 2218, both at $z \simeq 2.5$, were detected in Lyman α absorption. We measured secure redshifts for 51 other sources using other emission lines, primarily [O II], [O III], and H α . These data are useful for further constraining the cluster mass models, and will be presented in a separate paper (Richard et al., in prep.).

⁴ IRAF is distributed by the National Optical Astronomy Observatories, which are operated by the Association of Universities for Research in Astronomy, Inc., under cooperative agreement with the National Science Foundation.

6. SURVEY ANALYSIS

In this section we compute the number density of Lyman α emission-line galaxies in our survey as a function of Lyman α line luminosity, L . To accomplish this we first determine the effective volume of the survey as a function of the luminosity and redshift of a source.

6.1. Survey Volume

A location in our survey volume is characterized both by location on the sky, Ω , and a redshift, z . The differential volume element located at position (Ω, z) in our survey is

$$dV_c(\Omega, z) = \frac{1}{\mathcal{M}(\Omega, z)} \left[\frac{dl_c(z)}{dz} dz \right] \times [D_c^2(z) d\Omega]. \quad (2)$$

The first factor corrects for the lensing effect, which decreases the area surveyed. The second factor is the comoving length of the volume element along the line of sight, with

$$\frac{dl_c(z)}{dz} = \frac{c}{H_0 [\Omega_m(1+z)^3 + \Omega_\Lambda]^{3/2}} \quad (3)$$

(we have assumed a flat universe). The third factor is the comoving transverse area of the volume element, with

$$D_c(z) = \int_0^z \frac{dl_c(z')}{dz'} dz' \quad (4)$$

(subscript “c” denotes that the quantity is measured in comoving coordinates, which we use throughout).

Every volume element of our survey is characterized by a limiting Lyman α line luminosity, $L_{\text{lim}}(\Omega, z)$; a source with Lyman α line luminosity L will be detected in our survey provided it resides in a volume element with $L_{\text{lim}}(\Omega, z) \leq L$. The limiting luminosity of a volume element depends on the magnification (due to lensing by the foreground cluster), $\mathcal{M}(\Omega, z)$, the limiting observed Lyman α line flux $f_{\text{lim}}(z)$, and a slit transmission function, $T(\Omega)$,

$$L_{\text{lim}}(\Omega, z) = \frac{4\pi(1+z)^2 D_c^2(z)}{T(\Omega)} \frac{f_{\text{lim}}(z)}{\mathcal{M}(\Omega, z)}. \quad (5)$$

6.1.1. Magnification, $\mathcal{M}(\Omega, z)$

The magnification due to lensing by a given cluster is a function of both position and redshift. The references for the cluster mass models are given in Table 1. These models were run through the LENSTOOL software (Kneib 1993) to generate the magnification as a function of redshift at every position in the survey. In practice the area of the survey was divided into parcels of sky of length $0.8''$ and width equal to the slit width, and the magnification was calculated at the center of each parcel. The magnification at each position was sampled at nine redshifts, and the magnification at a particular redshift found by interpolation.

Figure 6 shows the magnification as a function of position along a slit observed in Abell 2218, for two different redshifts. The magnification at a given position is a weak function of redshift for magnification values less than ~ 100 (94% of the survey area), because the angular diameter distance between the cluster and the source changes by less than 25% over the source redshift

range $4.5 < z < 6.7$. Very near the critical lines magnification is a stronger function of redshift. Our survey maps sky by observing adjacent slit positions, so errors associated with interpolating the highest magnification $\mathcal{M}(\Omega, z) > 100$ points should not be important in our estimate of the survey volume.

Figure 7 is a cumulative histogram of the magnification factor over the survey; the area surveyed as a function of magnification is very weak function of redshift, even at the highest magnifications. About half of the area we surveyed is magnified by at least a factor of 10, with the lower magnification values coming from area at the ends of the slits, because most strong-lensing clusters subtend a size less than the slit length ($175''$) on the sky (see Fig. 2).

6.1.2. Limiting Lyman α line flux, $f_{\text{lim}}(z)$

We define our limiting Lyman α line flux as the signal in an aperture of $1.3''$ by 7.7 \AA that exceeds 5 times the root-mean-square fluctuations (noise) in apertures of that size, i.e., a $5\text{-}\sigma$ limit. The spatial dimension of the aperture was chosen to be roughly matched to the seeing, and the spectral dimension was chosen match the expected line-width of high-redshift Lyman α emission from galaxies, $\sim 300 \text{ km s}^{-1}$. If a source is larger than our aperture, which is especially possible along the spatial direction if the source is strongly lensed, then we will not be as sensitive to that source as we estimate.

We assumed that the sky noise was constant over the length of the slit at fixed wavelength. This allowed us to include the non-Poisson contribution to the noise level from fringing features, which dominated the noise on strong sky lines. All three of our confirmed $z > 4.5$ detections were more than $5\text{-}\sigma$ detections, but we found that visual inspection generated candidates (some of which were subsequently confirmed as bona fide emission lines) with fluxes below the $5\text{-}\sigma$ limit; in particular, one of the likely candidates at $z > 4.5$ is just at the $5\text{-}\sigma$ limit. Thus a $5\text{-}\sigma$ limit should be appropriate for the calculation of our survey volume.

The limiting line flux varies as a function of wavelength due to the wavelength dependence of the atmospheric absorption and the sensitivities of the telescope and instrument, but the largest dependence is due to the strong variation in atmospheric emission from OH airglow lines (except at $\lambda \gtrsim 9300 \text{ \AA}$, where the sharp drop in instrumental sensitivity dominates). Figure 8 shows $f_{\text{lim}}(z)$ for the slit pointing illustrated in Fig. 6, a 2000 sec observation under photometric conditions. We compute $f_{\text{lim}}(z)$ by simple conversion of the observed wavelength into the corresponding redshift for Lyman α to be observed at that wavelength.

Approximately half of our survey data were taken in non-photometric conditions. We account for this by dividing the limiting line flux measured from the observations by our best estimate of the sky transparency during the exposure. During some exposures we have sequences of guide-camera observations that were used to measure relative transparency between observations, and in some cases absolute transparency when photometric guide-camera images were available. In other cases we rely on observation log notes based on the count rate of the guide star as reported by the telescope operator.

6.1.3. Slit transmission, $T(\Omega)$

The slit widths used in our survey, originally $0.7''$ and later $1''$, are comparable in size to the seeing disk. Consequently the transverse distance of a source from the center-line of the slit has a small impact on the source's observability: objects in the center of the slit are easier to detect than objects at the slit edge. Since the absolute calibration was performed with respect to standard stars in the center of the slit, we compute the fraction of light transmitted through the slit as a function of transverse position on the slit (ignoring objects outside of the slit, as they will in general fall on another slit), with respect to an object at the center of the slit,

$$T(\Omega) = \frac{\text{erf}\left[\frac{w+2x}{s}\beta\right] + \text{erf}\left[\frac{w-2x}{s}\beta\right]}{2 \text{erf}\left[\frac{w}{s_0}\beta\right]}. \quad (6)$$

Here w is the slit width, s is the seeing full-width at half maximum (FWHM) during survey observations, s_0 is the seeing FWHM during standard star observations, $x(\Omega)$ is the transverse distance of the source from the center of the slit, and $\beta \equiv \sqrt{\ln(2)}$. The minimum value of $T(\Omega)$ in our survey is about 0.8, so it has a minor effect on the computation of $L_{\text{lim}}(\Omega, z)$.

6.2. Volume as a function of source redshift and luminosity

The total volume of our survey sensitive to a source of Lyman α line luminosity L is the integral over all volume elements in the survey with $L_{\text{lim}}(\Omega, z) \leq L$,

$$V_c(L) = \int_{\Omega} \int_z dV_c(\Omega, z) H[L - L_{\text{lim}}(\Omega, z)], \quad (7)$$

where $H(y)$ is the step function defined with $H(y \geq 0) = 1$.

Figure 9 shows the redshift distribution of our survey volume as a function of $L_{\text{lim}}(\Omega, z)$. The general slight decrease toward high redshift is due to the evolution of the line element with redshift, and the modulation is due to the wavelength-dependent limiting line flux (see Fig. 8).

We divide our survey arbitrarily into two redshift bins, $4.6 < z < 5.6$, and $5.6 < z < 6.7$. There is no natural binning choice, but by breaking our survey at $z = 5.6$ we retain almost equal survey volume (at the brightest luminosities) in each bin. However this places all three of our confirmed high-redshift detections into the $4.6 < z < 5.6$ bin, and none in the $5.6 < z < 6.7$ bin. If we had broken the bins at $z = 5.5$, the number density in the lower redshift bin would decrease, and the number density in the higher-redshift would increase, that is, the removal or inclusion of a source substantially outweighs the change in volume associated with changing the redshift binning.

In Fig. 10 we plot the survey volume sensitive to a source of luminosity L for each of our two redshift bins (represented by the two different symbols). At high luminosities there is no dependence of the survey volume on luminosity, because sources at such high luminosities are so bright that we would detect them at any magnification factor or redshift in our survey. At $L = 10^{42} \text{ erg s}^{-1}$ the high-redshift bin has less volume because of the stronger sky lines at longer wavelengths (see Figs. 8 and 9) and larger luminosity distance compared to the low-redshift

bin. At lower luminosities the survey volume for both bins falls off steadily and similarly. This is because only strongly magnified volume elements contribute to the survey volume, and the number of volume elements at a given magnification is not sensitive to redshift (Fig. 7).

6.3. Number Density

Our survey detected three confirmed and two likely $z > 4.5$ sources, so to estimate a relatively robust number density parameter, and for comparison with other surveys, we compute a cumulative number density of sources. We construct the cumulative number density at each value of the Lyman α line luminosity L (in each redshift bin) by evaluating the survey volume at that luminosity (see above), and then counting the number of detected sources brighter than L in the survey volume.

Figure 11 shows $n(> L)$, the number density of sources with Lyman α line luminosities greater than L , for our two redshift bins, *considering only the three confirmed sources*. There are only upper limits at $L \geq 10^{43} \text{ erg s}^{-1}$ because although all three detected sources are in the survey volume, none was that luminous. Our most luminous source is $7.4 \times 10^{42} \text{ erg s}^{-1}$, so the first data point appears at $L = 10^{42.5} \text{ erg s}^{-1}$ (in the low-redshift bin). All three of our confirmed detections contribute to the $L = 10^{41.5} \text{ erg s}^{-1}$ point because all are brighter than that limit, and each would have been detected even if its luminosity were only $10^{41.5} \text{ erg s}^{-1}$. In contrast at $L = 10^{41} \text{ erg s}^{-1}$, all three confirmed detections are still brighter than this luminosity, but only one is located inside the $L = 10^{41} \text{ erg s}^{-1}$ survey volume. At yet fainter luminosities we are back to upper limits because none of the three confirmed detections would have been discovered if it were fainter than $10^{41} \text{ erg s}^{-1}$.

In our high-redshift bin we have no detections, and thus can provide only upper limits at all luminosities. It is clear that though we can rule out a strong increase in the number counts of Lyman α emitters at $5.6 < z < 6.7$ compared to $4.6 < z < 5.6$, we cannot further constrain the number-count evolution. In particular, our results are consistent with no evolution or a decrease with increasing redshift in the Lyman α source counts as a function of redshift over $4.6 < z < 6.7$.

All upper limits and error bars in Fig. 11 are 95% confidence limits calculated using Poisson statistics. We have conceptually divided our survey into sub-surveys sensitive down to different Lyman α line luminosities, but these sub-surveys are not independent (and in fact highly correlated). If, for example, a theoretical curve passed just through the upper error bars of two points, our data would indicate roughly a 95% inconsistency, not a 99.8% inconsistency.

The right and top axes of Fig. 11 are labeled with unit conversions of the left and bottom axes, assuming the data fall at $z = 5$. These serve to allow a rough reference of our results to be easily read off in the other units commonly used to describe the abundance of Lyman α emission-line galaxies. The right and top axes are inapplicable to our high-redshift bin upper limits.

Figure 11 shows $n(> L)$, the number density of sources with Lyman α line luminosities greater than L , for our two redshift bins, *considering all five confirmed and likely sources*. Since we added detections while keeping the survey volume fixed, the number densities increased. The

number densities of this sample are still marginally consistent with the 95% confidence limits from Fig. 11.

7. COMPARISON WITH OTHER OBSERVATIONS AND WITH THEORY

7.1. Comparison with Other Observations

In Table 4 we present parameters inferred from our survey and existing $z \sim 5$ galaxy surveys. The first five entries in the table describe our survey, divided by redshift bin and sub-survey limiting Lyman α line luminosity. The remaining surveys above the horizontal rule are other Lyman α emission-line surveys. Surveys below the horizontal rule are Lyman-break galaxy surveys, described later in this section.

There are two entries in the number of sources column for each row corresponding to our data. The first number is the total number of confirmed and likely Lyman α sources in that sub-survey, and the second number, in parentheses, in the number of those that are confirmed. We report the corresponding number densities analogously in the density column.

The limiting luminosity, volume, and number density of each of the previously published Lyman α emission-line surveys appearing in Table 4 do not always appear in the corresponding reference. As necessary we have used the published information to calculate those values ourselves (for example, converting a limiting line flux and redshift into a limiting line luminosity). We expect that the final results published by the groups may differ somewhat. In particular, there may be a publication bias toward surveys with discoveries, so it is possible there is some bias in the data presented toward higher number density. We have included only systematic Lyman α emission surveys, because reconstructing the survey volumes of published serendipitous discoveries was not possible.

Fig. 13 plots the data from the $4.6 < z < 5.6$ bin of our survey (as solid circles) with the data from the other Lyman α surveys listed in Table 4 (open squares). Note that these points are in general from different redshifts, and no redshift correction has been applied. The error bars shown are 95% confidence limits assuming Poisson errors.

A comparison of our data with published results shows that, by utilizing strong lensing, we have provided meaningful upper limits on the population of Lyman α emission-line galaxies two orders of magnitude fainter than previous surveys, in addition to providing confirmed data one order of magnitude fainter. With existing observational facilities, lensed surveys are the only way to probe to such depth.

At $L = 10^{42.5} \text{ erg s}^{-1}$, where our survey overlaps other Lyman α surveys, there is marginal consistency between our data and published results. Most of the other Lyman α surveys are narrow-band photometric surveys (in particular the three surveys with > 10 sources in Table 4), where the points plotted do not represent confirmed sources, but rather photometric candidates corrected for the spectroscopic success rate of a small sample. As noted previously this figure represents data reported inhomogeneously, so some of the scatter may be related to the different redshift ranges and Lyman α equivalent-width criteria of the surveys, as well as errors in contamination estimation and possible errors in

our interpretation of published information.

We detected no sources at $z > 5.6$. This is marginally inconsistent with existing data of source densities at $z = 5.7$ and $z = 6.5$. However, our lack of sources at $z > 5.6$ compared to other surveys is qualitatively consistent with our smaller number density of $4.6 < z < 5.6$ sources at $L = 10^{42.5} \text{ erg s}^{-1}$.

For comparison, we have plotted results from four $z \sim 5$ Lyman-break galaxy (LBG) surveys (Stanway, Bunker, & McMahon 2003; Yan, Windhorst, & Cohen 2003; Iwata et al. 2003; Fontana et al. 2003; Lehnert & Bremer 2002). The parameters for these surveys are listed in Table 4, below the horizontal rule. Again we have converted published data into number density as necessary, and taken a further step to plot those points on a Lyman α line luminosity scale: the LBG survey limit was converted into a rest-frame UV continuum limit, then into a star-formation rate using the relation of Kennicutt (1998), then into a Lyman α line luminosity assuming $1 \text{ M}_{\odot} \text{ yr}^{-1}$ of star formation produces $10^{42} \text{ erg s}^{-1}$ in the Lyman α line (Kennicutt 1998, after converting $\text{H}\alpha$ luminosity into Lyman α luminosity). No unmitigated conclusions can be drawn from this comparison, though it is intriguing that the $z \sim 5$ LBG surveys may be discovering the same population as the Lyman α emission-line galaxies, if the Lyman α line is typically 1/3 the value expected based on the UV continuum SFR. This is similar to the ratio observed in the $z = 5.7$ sample of Lyman α emitters of Ajiki et al. (2003) and in two galaxies at $z = 6.5$ by Hu et al. (2002b) and Kodaira et al. (2003). However, four of six confirmed $4.8 < z < 5.8$ galaxies selected by the Lyman-break technique by Lehnert & Bremer (2002) have Lyman α line fluxes less than 10% of the values naively predicted from their UV continuum SFRs.

7.2. Comparison with Theoretical Models

First we compare our results with the Lyman α emitter model of Haiman & Spaans (1999), who predicted the abundance of Lyman α emitters over a range of redshifts and luminosities. In Figs. 13 and 14 we plot the predictions of their fiducial model at $z = 5$ as a long-dashed curve from $\log_{10} L = 40.5$ to 42.5. The shape of the luminosity function predicted by Haiman & Spaans (1999) is similar to our observed points, but their fiducial model predicts approximately an order of magnitude more sources than we find. Their models could be reconciled with our data by adopting mass-dependent values of the star-formation efficiency or covering fraction of dusty clouds inside the galaxies.

As a basis for comparing our results with a simple theoretical model, in Figs. 13 and 14 we re-plot the luminosity function from Fig. 1 (converted into cumulative form), assuming no suppression of the SFR in low-mass halos. This simple interpretation of the Lyman α luminosity function relates the number density of galaxies to dark matter halos. We then converted baryons within those dark matter halos into stars, and stellar ionizing light into Lyman α photons. Unlike Haiman & Spaans (1999) we made no attempt to model the radiative transfer of the Lyman α photons.

Specifically, we assumed that 10% of the baryons in each halo were converted into stars every halo dynamical

time (defined as the ratio of the halo virial radius to the halo circular velocity at the virial radius). The Hubble time at $z = 5$ is roughly 10 times longer than the halo dynamical time, thus it is possible for such halos to maintain steady star formation at this rate. Star-formation rate was converted into an ionizing-photon rate using a Salpeter IMF with 1/20 solar metallicity (Leitherer et al. 1999). We assumed that 10% of the ionizing photons escape the emitting galaxy, and that 2/3 of the remaining photons are converted into Lyman α emission.

The luminosity function predicted by this simple model provides a poor fit to our data. In the context of the model, it is instructive to think of two modifications that would make the predicted luminosity function more closely match our data. The first is to decrease the efficiency factors used to convert halo mass to Lyman α luminosity in a given halo. Alternately, the model curve could be brought into agreement with our data if the efficiency factor for the production of Lyman α was correct for a fraction of halos, but the rest had no observable Lyman α emission at the time of observation.

There are three efficiencies that contribute to the overall conversion of halo mass into Lyman α luminosity, namely the fraction of baryons converted into stars per halo dynamical time, the stellar emissivity of ionizing photons, and the fraction of ionizing photons observed as Lyman α emission. Lowering the combined efficiency by 1.5–2 orders of magnitude would bring the model luminosity function into close agreement with our data. There is some difference in the shape of the curve compared to our data, but this difference is not significant.

In the case where only a fraction of halos contain Lyman α emitters, we would require about 1% of halos to contain emitters at any given time. This could be because, in contrast to the simple model we described, star formation is episodic in nature. In addition, there could be a timescale associated with the escape of Lyman α photons, such that, for example, dust extinguishes Lyman α emission at the beginning of a starburst, but eventually the dust is expelled and the Lyman α emission line becomes visible (e.g., Shapley et al. 2003). If only some halos contain galaxies, for whatever reason, then this formalism of assuming only a fraction of halos contain Lyman α emitters can also be used, where the fraction now represents a filling factor, rather than a duty cycle.

The resolution of the discrepancy between our data and the model curve has important implications for the mass of the halos that contain the Lyman α emitters. If we over-estimated the Lyman α photon production efficiency in our model, then the association between halo mass and Lyman α emitter expressed in Figs. 13 and 14 is not correct: the halo mass of our population of emitters at $L \simeq 10^{41.5} \text{ erg s}^{-1}$ should be $\sim 10^{11} M_{\odot}$. This is the largest mass that could be inferred for this population, assuming a maximum of one Lyman α emitter per halo. From the arguments of Section 3, we may expect that halos with masses $\gtrsim 10^{10} M_{\odot}$ to form stars roughly similarly to one another, i.e., though negative feedback may be important in regulating star formation, it is ineffective in halos this massive. Consequently, for this low-efficiency, high halo-mass solution to the discrepancy, we expect that our data should follow the shape of the dark-matter halo mass function, which they do.

In contrast, if we resolve the discrepancy between the model and our data by assuming that the efficiency we calculated is correct for a fraction of halos, and the rest are empty of Lyman α emission, then the mass association in Figs. 13 and 14 is correct. This implies a halo mass of only $\sim 10^{9.5} M_{\odot}$ for our Lyman α emitters at $L \simeq 10^{41.5} \text{ erg s}^{-1}$. Depending on the characteristic mass scale where negative feedback becomes a dominant process, the Lyman α luminosity function may already deviate from the shape of the mass function at $\sim 10^{9.5} M_{\odot}$ (see Fig. 1). Our data are slightly flatter than the mass function, and consistent with any of the luminosity functions plotted in Fig. 1.

Our theoretical interpretation so far has relied exclusively on our data, which is consistent with the shape of the relevant halo mass function. However, if we consider all of the available Lyman α data, there is some evidence for a flatter Lyman α luminosity function. The heterogeneous nature of the Lyman α survey data plotted in Figs. 13 and 14 makes it difficult to draw firm conclusions, but a combination of data at $L \gtrsim 10^{42.5} \text{ erg s}^{-1}$ suggests that our data point at $L = 10^{41.5} \text{ erg s}^{-1}$ may be 0.5–1 dex lower than an extrapolation of the Lyman α luminosity function from higher luminosity, assuming the luminosity function shape matches the mass function shape. Thus we conclude that our data, in combination with other Lyman α surveys, suggest that strong negative feedback is suppressing the star-formation rate, and thus Lyman α luminosity, in our sources.

Hamana et al. (2003) used clustering data to estimate the mass of the halos containing Lyman α emitters at $z = 4.9$. They concluded that the characteristic halo mass of those sources is $5 \times 10^{12} M_{\odot}$ (Shimasaku et al. 2003 find a halo mass of $\sim 10^{12} M_{\odot}$ for similar $z = 4.9$ emitters on the basis of a large-scale structure feature in their survey). This conclusion would support the low-efficiency, high halo-mass solution to the difference between our model luminosity function and our data. However, the number density of $z = 4.9$ emitters is larger, by about a factor of five to ten, than the number density of $10^{12} M_{\odot}$ halos (Hamana et al. 2003). This implies, contrary to our assumption above, that there is more than one Lyman α source per halo. The virial radius of a $z = 5$, $10^{12} M_{\odot}$ halo is $8.5''$, so multiple sources inside a single halo may be observed as separate sources, though this should create a very distinct signature in the spatial distribution of sources (or extended nature, if the sources are unresolved) that has not been reported by other Lyman α emitter surveys.

While current information on the masses of Lyman α emitter halos is still limited, progress will continue to be made at $L \gtrsim 10^{42.5} \text{ erg s}^{-1}$ by large Lyman α surveys. Unfortunately, surveys for low-luminosity Lyman α emitters will not provide sufficient survey area for clustering studies in the near future. Lensed surveys such as ours, in particular, do not lend themselves to easy clustering analysis, because the contiguous survey volume is very complex and limited in size by the mass of the lensing foreground cluster. As an aside we comment that Poisson errors dominate the uncertainty in the number densities plotted in Figs. 11 and 12 (and Figs. 13 and 14 for our survey), assuming the maximum mass for the halos containing our emitters (i.e., every halo contains a source; see above for a caveat), and using the clustering formal-

ism of Mo & White (2002).

Until the advent of large-area, low-luminosity Lyman α surveys, the only constraint on the mass of the halos containing the emitters, and thus the only path toward understanding the suppression of star-formation in low-mass halos, lies in detecting source populations with high number densities, such that the halo mass function, and the assumption that there is at most one source per halo, can be used to infer a maximum halo mass for the population of Lyman α emitters. This is strong motivation for future surveys to continue to use strong lensing to survey small volumes to considerable depths for faint, Lyman α emitting sources.

8. SUMMARY

We performed a systematic survey for Lyman α emission at $2.2 < z < 6.7$ using strong lensing from intermediate-redshift clusters of galaxies to boost our survey sensitivity to unprecedented depths. We detected three confirmed and two likely Lyman α emitting galaxies at $4.7 < z < 5.6$, with Lyman α line luminosities of $2.8 \times 10^{41} \text{ erg s}^{-1} < L < 7.4 \times 10^{42} \text{ erg s}^{-1}$. Our survey covered 4.2 arcmin^2 on the sky, with a maximum volume of $4 \times 10^4 \text{ Mpc}^3$ over $4.6 < z < 6.7$. We find no evidence for redshift evolution of the number density of Lyman α emitting galaxies between $z \sim 5$ and $z \sim 6$, though our data are also consistent with a decrease in number density with increasing redshift.

We present the first meaningful constraints on the the luminosity function of Lyman α emitters at $4.6 < z < 5.6$ over the Lyman α luminosity range $10^{40} \text{ erg s}^{-1} < L < 10^{42} \text{ erg s}^{-1}$, corresponding to inferred star-formation

rates of $0.01\text{--}1 \text{ M}_{\odot} \text{ yr}^{-1}$. From a consideration of the number density of dark-matter halos, we conclude that our population of sources at $L \sim 10^{41.5} \text{ erg s}^{-1}$ resides in halos of mass $\lesssim 10^{11} \text{ M}_{\odot}$.

Our number density data are consistent with a Lyman α luminosity function with the same shape as the halo mass function, but a consideration of all available Lyman α survey data implies that we have observed a flattening of the Lyman α luminosity function with respect to the halo mass function. We may have detected evidence of the suppression of star-formation in low-mass halos at high redshift, as predicted by theoretical models of galaxy formation.

We thank Alice Shapley for many enlightening conversations. We thank Graham Smith for help with mass modeling of some clusters. We also thank Pieter van Dokkum, Andrew Firth, and Tommaso Treu for help obtaining and reducing the observations.

We gratefully acknowledge the helpful staff at Keck Observatory, and the teams responsible for the creation and maintenance of the telescopes and instruments there.

The authors recognize and acknowledge the very significant cultural role and reverence that the summit of Mauna Kea has always had within the indigenous Hawaiian community. We are most fortunate to have the opportunity to conduct observations from this mountain.

MRS acknowledges the support of NASA GSRP grant NGT5-50339. JPK acknowledges support from CNRS and Caltech.

REFERENCES

- Ajiki, M. et al. 2003, ApJ, accepted, astro-ph/0307325
 Barger, A. J., Cowie, L. L., Capak, P., Alexander, D. M., Bauer, F. E., Brandt, W. N., Garmire, G. P., & Hornschemeier, A. E. 2003, ApJ, 584, L61
 Barkana, R. & Loeb, A. 1999, ApJ, 523, 54
 Barkana, R. & Loeb, A. 2003, Nature, 421, 341
 Becker, R. H. et al. 2001, AJ, 122, 2850
 Benson, A. J., Lacey, C. G., Baugh, C. M., Cole, S., & Frenk, C. S. 2002a, MNRAS, 333, 156
 Benson, A. J., Frenk, C. S., Lacey, C. G., Baugh, C. M., & Cole, S. 2002b, MNRAS, 333, 177
 Bézecourt, J., Kneib, J. P., Soucail, G., & Ebbels, T. M. D. 1999, A&A, 347, 21
 Blandford, R. D. & Narayan, R. 1992, ARA&A, 30, 311
 Dekel, A. & Silk, J. 1986, ApJ, 303, 39
 Dey, A., Spinrad, H., Stern, D., Graham, J. R., & Chaffee, F. H. 1998, ApJ, 498, L93
 Djorgovski, S. G., Castro, S., Stern, D., & Mahabal, A. A. 2001, ApJ, 560, L5
 Eisenstein, D. J. & Hu, W. 1999, ApJ, 511, 5
 Ellis, R. S., Santos, M. R., Kneib, J.-P., & Kuijken, K. 2001, ApJ, 560, L119
 Fan, X. et al. 1999, AJ, 118, 1
 Fan, X. et al. 2000, AJ, 119, 1
 Fan, X. et al. 2001, AJ, 121, 31
 Fan, X., Narayanan, V. K., Strauss, M. A., White, R. L., Becker, R. H., Pentericci, L., & Rix, H. 2002, AJ, 123, 1247
 Fontana, A., Poli, F., Menci, N., Nonino, M., Giallongo, E., Cristiani, S., & D’Odorico, S. 2003, ApJ, 587, 544
 Franx, M., Illingworth, G. D., Kelson, D. D., van Dokkum, P. G., & Tran, K. 1997, ApJ, 486, L75
 Frye, B., Broadhurst, T., & Benítez, N. 2002, ApJ, 568, 558
 Gallego, J., Zamorano, J., Aragon-Salamanca, A., & Rego, M. 1995, ApJ, 455, L1
 Gnedin, N. Y. 2000, ApJ, 542, 535
 Haiman, Z. 2002, ApJ, 576, L1
 Haiman, Z. & Spaans, M. 1999, ApJ, 518, 138
 Hamana, T., Ouchi, M., Shimasaku, K., Kayo, I., & Suto, Y. 2003, MNRAS, submitted, astro-ph/0307207
 Harris, W. E. 1996, AJ, 112, 1487
 Hu, E. M., Cowie, L. L., & McMahon, R. G. 1998, ApJ, 502, L99
 Hu, E. M., McMahon, R. G., & Cowie, L. L. 1999, ApJ, 522, L9
 Hu, E. M., Cowie, L. L., McMahon, R. G., Capak, P., Iwamuro, F., Kneib, J.-P., Maihara, T., & Motohara, K. 2002a, ApJ, 568, L75
 Hu, E. M., Cowie, L. L., McMahon, R. G., Capak, P., Iwamuro, F., Kneib, J.-P., Maihara, T., & Motohara, K. 2002b, ApJ, 576, L99
 Ivison, R. J. et al. 2002, MNRAS, 337, 1
 Iwata, I., Ohta, K., Tamura, N., Ando, M., Wada, S., Watanabe, C., Akiyama, M., & Aoki, K. 2003, PASJ, 55, 415
 Kennicutt, R. C. 1998, ARA&A, 36, 189
 Kneib, J.-P. 1993, Ph.D. Thesis
 Kneib, J.-P., Ellis, R. S., Smail, I., Couch, W. J., & Sharples, R. M. 1996, ApJ, 471, 643
 Kodaira, K. et al. 2003, PASJ, 55, L17
 Krauss, L. M. & Chaboyer, B. 2003, Science, 299, 65
 Lehnert, M. D. & Bremer, M. 2003, ApJ, accepted, astro-ph/0212431
 Leatherer, C. et al. 1999, ApJS, 123, 3
 Lilly, S., Tran, K., Brodwin, M., Crampton, D., Juneau, S., & McCracken, H. 2003, ApJ submitted, astro-ph/0304376
 Maier, C. et al. 2003, A&A, 402, 79
 Malhotra, S. & Rhoads, J. E. 2002, ApJ, 565, L71
 Martin, C. L. & Sawicki, M. 2003, ApJ, submitted
 Massey, P. & Gronwall, C. 1990, ApJ, 358, 344
 Mather, J. C. & Stockman, H. S. 2000, Proc. SPIE, 4013, 2
 Mo, H. J. & White, S. D. M. 2002, MNRAS, 336, 112
 Moore, B., Ghigna, S., Governato, F., Lake, G., Quinn, T., Stadel, J., & Tozzi, P. 1999, ApJ, 524, L19
 Neufeld, D. A. 1991, ApJ, 370, L85
 Oke, J. B. et al. 1995, PASP, 107, 375

- Osterbrock, D. E. 1989, *Astrophysics of gaseous nebulae and active galactic nuclei* (Mill Valley, CA: University Science Books)
- Ouchi, M. et al. 2003, *ApJ*, 582, 60
- Partridge, R. B. & Peebles, P. J. E. 1967, *ApJ*, 147, 868
- Pelló, R. et al. 1999, *A&A*, 346, 359
- Pettini, M., Madau, P., Bolte, M., Prochaska, J. X., Ellison, S. L., & Fan, X. 2003, *ArXiv Astrophysics e-prints*, 5413
- Press, W. H. & Schechter, P. 1974, *ApJ*, 187, 425
- Pritchett, C. J. 1994, *PASP*, 106, 1052
- Rhoads, J. E., Malhotra, S., Dey, A., Stern, D., Spinrad, H., & Jannuzi, B. T. 2000, *ApJ*, 545, L85
- Rhoads, J. E. & Malhotra, S. 2001, *ApJ*, 563, L5
- Rhoads, J. E. et al. 2003, *AJ*, 125, 1006
- Santos, M. R. 2003, *MNRAS*, submitted, astro-ph/0308196
- Scannapieco, E., Ferrara, A., & Broadhurst, T. 2000, *ApJ*, 536, L11
- Scannapieco, E. & Broadhurst, T. 2001, *ApJ*, 549, 28
- Schechter, P. 1976, *ApJ*, 203, 297
- Shapley, A. E., Steidel, C. C., Pettini, M., & Adelberger, K. L. 2003, *ApJ*, 588, 65
- Sheinis, A. I., Bolte, M., Epps, H. W., Kibrick, R. I., Miller, J. S., Radovan, M. V., Bigelow, B. C., & Sutin, B. M. 2002, *PASP*, 114, 851
- Sheth, R. K. & Tormen, G. 2002, *MNRAS*, 329, 61
- Shimasaku, K. et al. 2003, *ApJ*, 586, L111
- Smith, G. P. et al. 2002, *MNRAS*, 330, 1
- Smith, G. P., Edge, A. C., Eke, V. R., Nichol, R. C., Smail, I., & Kneib, J. 2003, *ApJ*, 590, L79
- Sokasian, A., Abel, T., & Hernquist, L. 2003, *MNRAS*, 340, 473
- Somerville, R. S. 2002, *ApJ*, 572, L23
- Songaila, A. 2001, *ApJ*, 561, L153
- Songaila, A. & Cowie, L. L. 2002, *AJ*, 123, 2183
- Spiegel, D. N. et al. 2003, *ApJ*, accepted
- Stanway, E. R., Bunker, A. J., & McMahon, R. G. 2003, *MNRAS*, 342, 439
- Stern, D. & Spinrad, H. 1999, *PASP*, 111, 1475
- Taniguchi, Y., Shioya, Y., Fujita, S. S., Nagao, T., Murayamaoya, T., & Ajiki, M. 2003, astro-ph/0306409
- van Dokkum, P. G. 2001, *PASP*, 113, 1420
- Weymann, R. J., Stern, D., Bunker, A., Spinrad, H., Chaffee, F. H., Thompson, R. I., & Storrie-Lombardi, L. J. 1998, *ApJ*, 505, L95
- Yan, H., Windhorst, R. A., & Cohen, S. H. 2003, *ApJ*, 585, L93

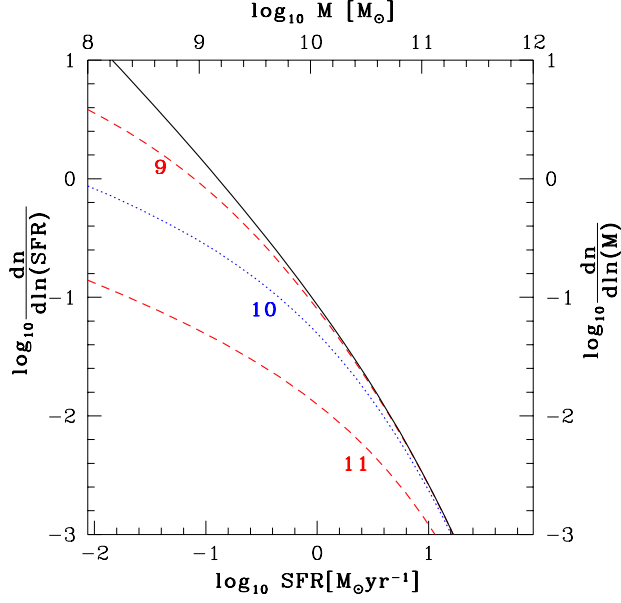


FIG. 1.— The star-formation rate function based on a dark matter halo model. The solid curve is the abundance (on the right axis) of halos at $z = 5$ as a function of the mass on the top axis. The bottom axis is a simple conversion of the halo mass into the expected star formation in that halo, so that the solid curve may also be read as a theoretical star-formation rate function using the bottom and left axes. The broken curves represent cases where star formation in low-mass halos has been suppressed; each is labeled with the logarithm of the mass scale below which suppression occurs. See Sections 3 and 7.2 for details.

TABLE 1
CLUSTERS SURVEYED

Cluster	Redshift	RA ^a	Dec ^b	Lens Model Reference
Abell 68	0.255	00 36 59	+09 09	(1)
Abell 370	0.375	02 37 18	-01 48	(2)
Abell 773	0.217	09 14 30	+51 55	(1)
Abell 963	0.206	10 17 09	+39 01	(1)
Abell 1689	0.183	13 09 00	-01 06	(3)
Cl1358.1+62.45	0.328	13 59 54	+62 31	(4)
Abell 2218	0.176	16 35 42	+66 19	(5,6)
Abell 2219	0.226	16 38 54	+46 47	(1)
Abell 2390	0.228	21 53 35	+17 40	(7)

^aunits of HH MM SS

^bunits of +DD MM

TABLE 2
LRIS SURVEY OBSERVATIONS

Date	Cluster	Position Angle ^a	Integration time ^b	Photometric?
Mar 2000	Abell 773	-46.8	20	Yes
	Abell 1689 #1	84.1	23	Yes
Apr 2001	Abell 1689 #2	43	10	Yes
	Abell 2218 #1	-44	10	Yes
	Cl1358	-15	12	Yes
Oct 2001	Abell 370 #1	-8	14	Yes
Apr 2002	Abell 963	3.6	14	No
	Abell 2218 #2	-49.2	14	No
May 2002	Abell 1689 #3	12.3	20	No
	Abell 2219	-69	14	No
Sep 2002	Abell 370 #2	1.7	14	No
	Abell 2390	-63	12	No
	Abell 68	-40	12	No

^ain degrees North through East

^bin ksec

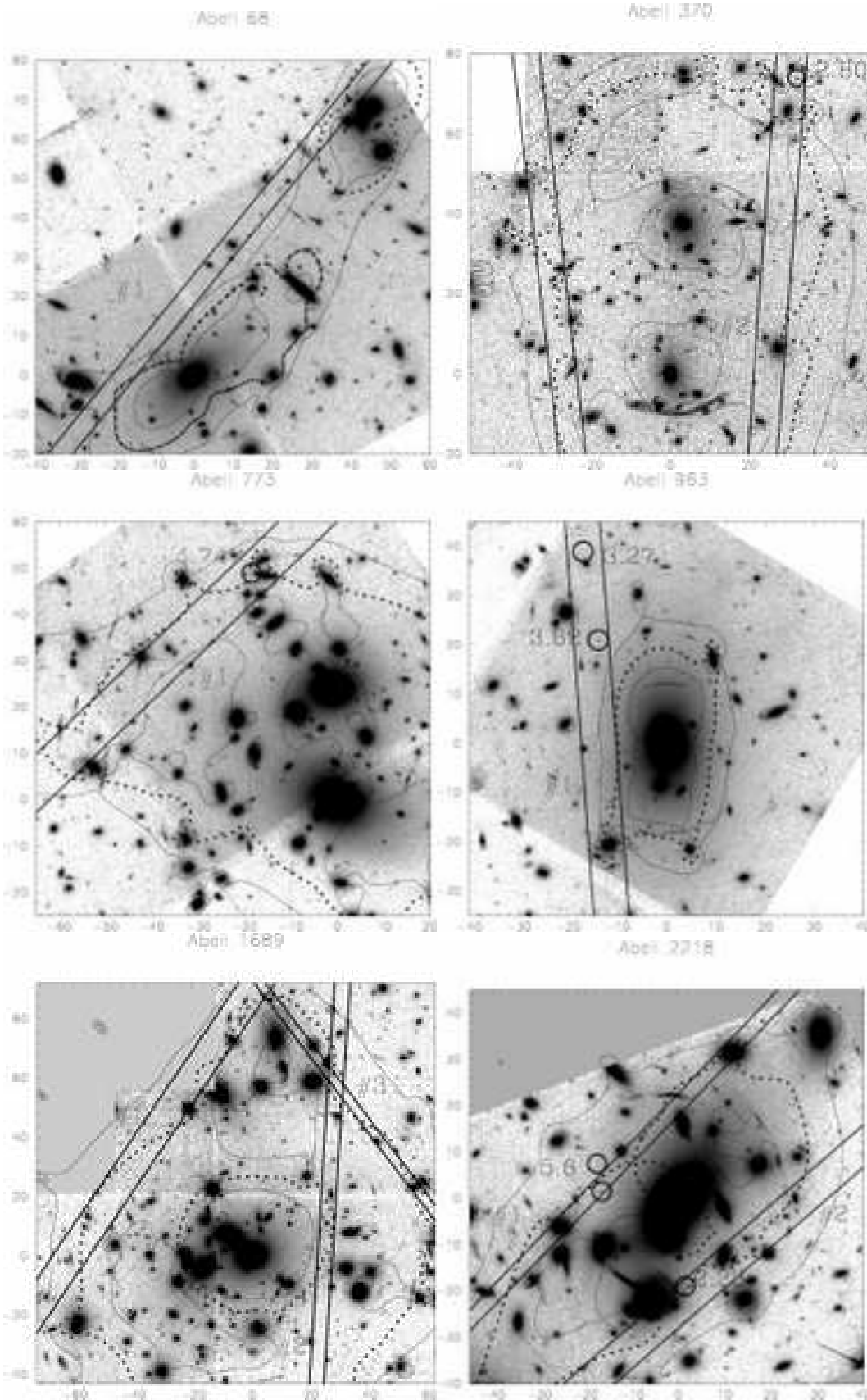


FIG. 2.— Survey geometry for a selected sample of our clusters. For each cluster, superposed on the *HST*/WFPC2 image are the critical lines for a source at $z = 5$ (dotted lines). The solid curves bound areas where the magnification for such a source exceeds a factor of 10. The regions bounded by parallel straight lines are the long-slit survey area. Numeric labels correspond to the key in Table 2. The axes are labeled in arcseconds. (upper left) Abell 68. (upper right) Abell 370. (middle left) Abell 773. (middle right) Abell 963. (lower left) Abell 1689. (lower right) Abell 2218.

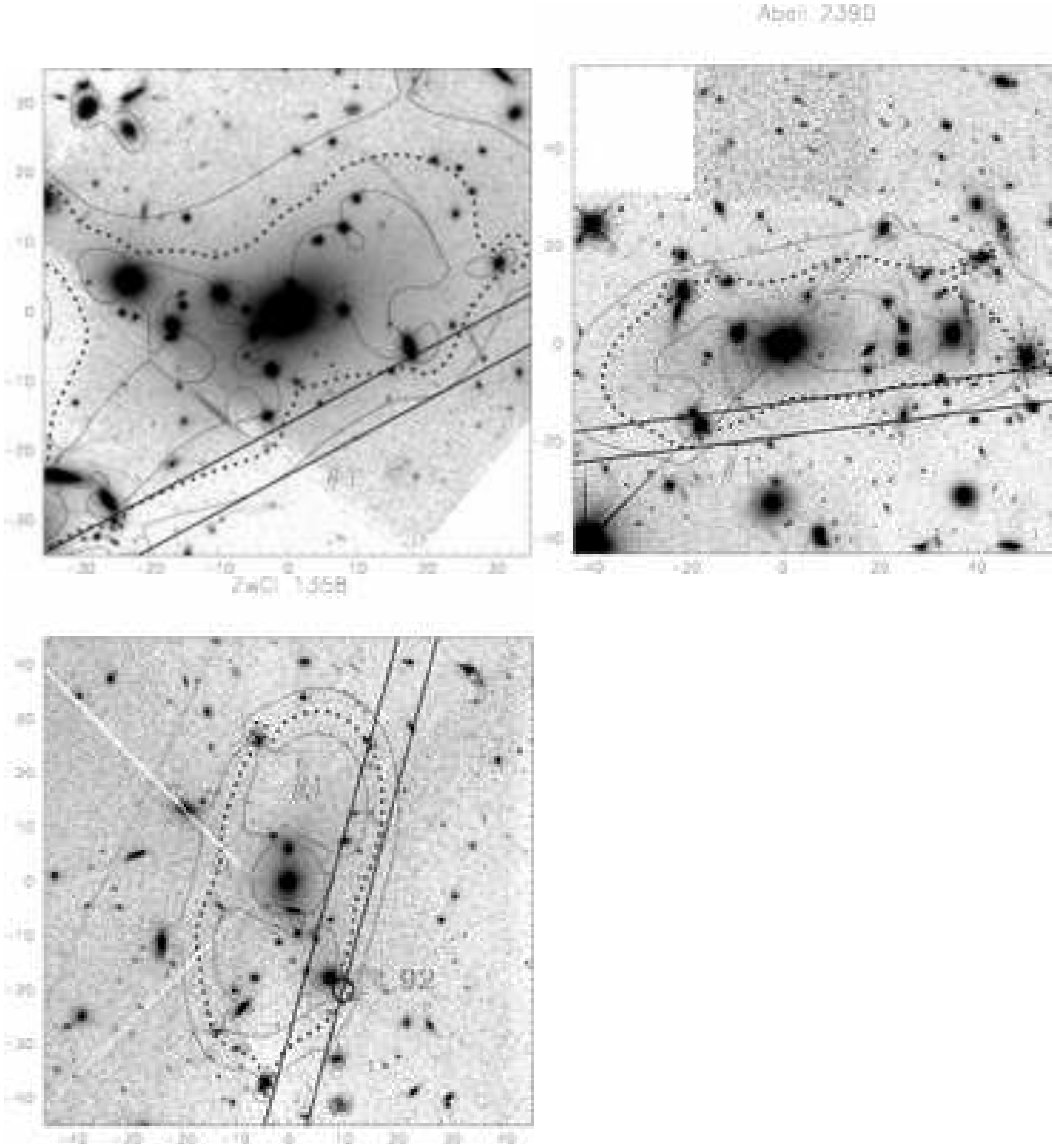


Fig. 2 cont.— (upper left) Abell 2219. (upper right) Abell 2390. (lower left) Cl1358.

TABLE 3
LYMAN α EMISSION-LINE CANDIDATES

Cluster ID	RA	Dec	λ^a	z^b	Flux ^c	Comments
Abell 370.1.f	2:39:50.60	-1:33:45.0	4628	2.80		confirmed (LRIS)
Abell 370.1.g	2:39:51.80	-1:35:57.6	4630	2.80		confirmed (Iverson et al. 2002)
Abell 963.1.cd	10:17:05.10	39:03:30.5	5191	3.27		confirmed (ESI)
Abell 963.1.efg	10:17:04.77	39:03:11.0	5617	3.62		confirmed (ESI)
Abell 1689.2.f	13:11:25.38	-1:20:52.4	7141	4.82	3.0	confirmed (Frye et al. 2002)
Abell 2218.1.a2	16:35:51.75	66:12:45.6	8001	5.58	4.4	confirmed (ESI, Ellis et al. 2001)
—	16:35:51.89	66:12:51.5				2nd image
Cl1358.1.ef	3:59:49.19	62:30:44.8	7205	4.92	10	confirmed (Franx et al. 1997)
Abell 773.1.e	9:17:55.31	51:44:26.6	6978	4.74	1.1	likely
Abell 963.1.d	10:17:04.45	39:01:47.1	7025	4.77	0.69	likely
Abell 2218.1.a1	16:35:45.25	66:13:26.4	4216	2.47		likely
Abell 2218.2.b	16:35:48.78	66:12:24.9	3928	2.23		likely

^aWavelength of emission line in units of \AA

^bSource redshift assuming emission line is Lyman α

^cObserved line flux (uncorrected for lensing, corrected for transparency) in units of $10^{-17} \text{ erg s}^{-1} \text{ cm}^{-2}$

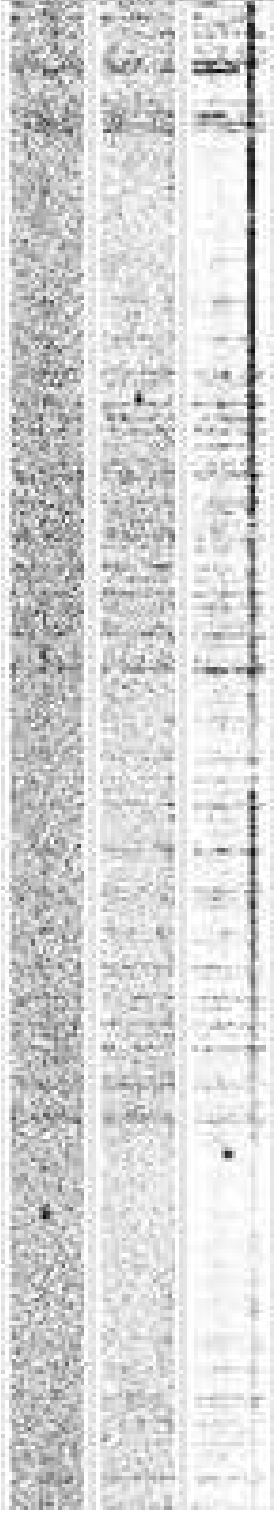


FIG. 3.— Two-dimensional spectra of the three confirmed $z > 4.5$ galaxies detected in the survey. The spectra, from left to right, are the $z = 4.89$ source in Abell 1689, the $z = 5.57$ source in Abell 2218, and the $z = 4.92$ source in Cl1358. The wavelength coverage in all the spectra is 6800 to 8430 Å, increasing bottom to top.

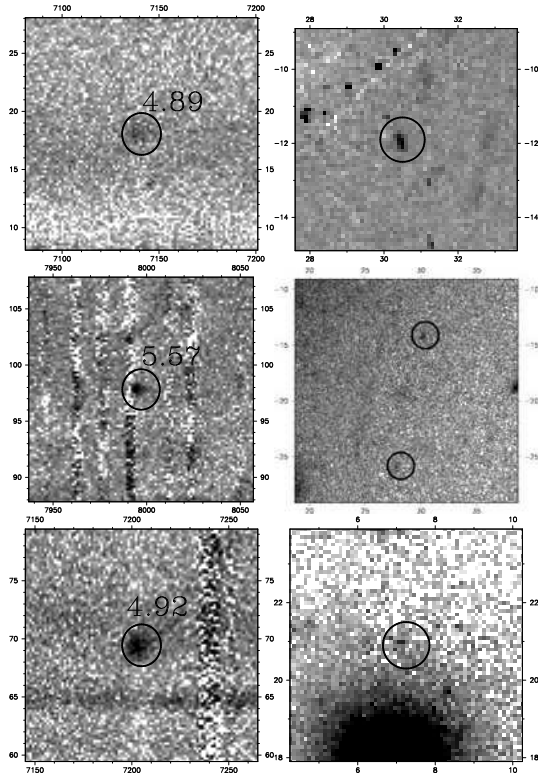


FIG. 4.— Two-dimensional spectra (left) and *HST* images (right) for our three confirmed Lyman α sources. In the spectra the horizontal axes are labeled in \AA , and the vertical axes in arcsec; the image axes are labelled in arcsec. (upper) Abell 1689.2.f. (middle) Abell 2218.1.a2. (lower) Cl1358.1.ef.

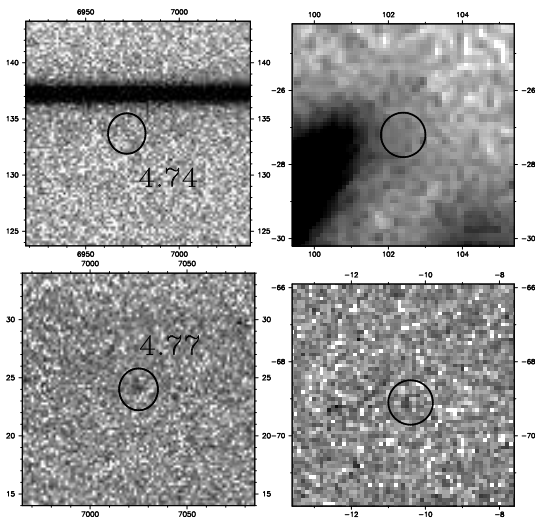


FIG. 5.— Two-dimensional spectra (left) and *HST* images (right) for our two likely Lyman α sources. In the spectra the horizontal axes are labeled in \AA , and the vertical axes in arcsec; the image axes are labelled in arcsec. (upper) Abell 773.1.e. (lower) Abell 963.1.d.

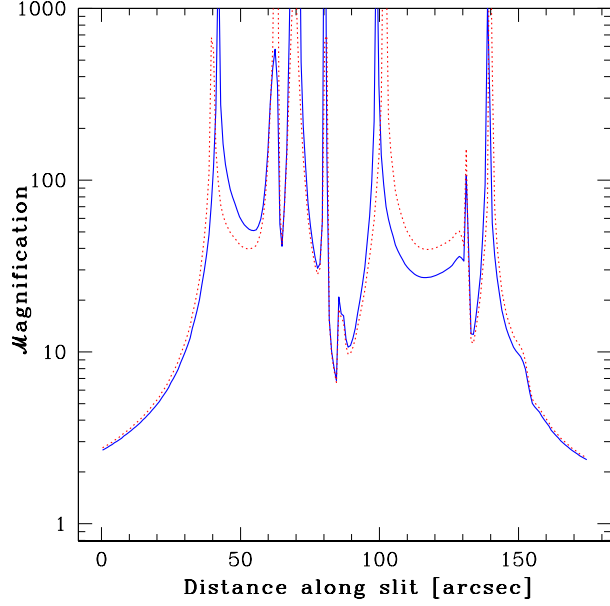


FIG. 6.— Magnification due to the cluster Abell 2218 of background sources, as a function of position and redshift. This figure shows the magnification factor at positions along a $175''$ longslit at one of our survey positions in Abell 2218 (within pointing “#1” in Fig. 2). The solid curve is for sources at $z = 4.3$, and the dotted curve is for sources at $z = 6.8$.

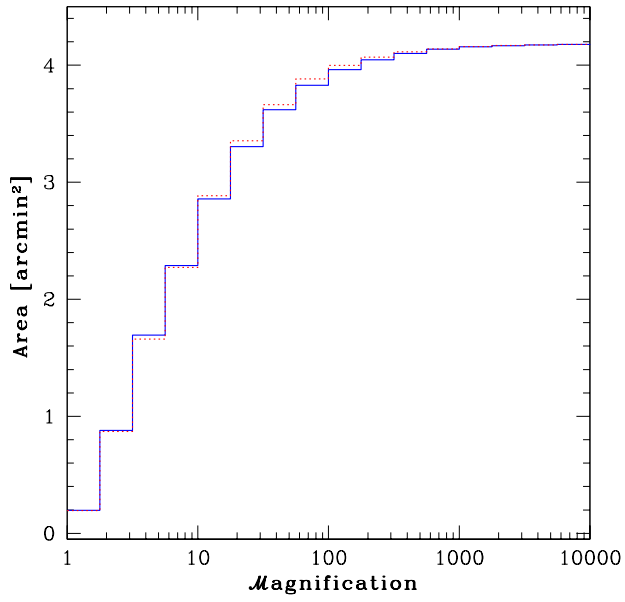


FIG. 7.— Cumulative histogram of the magnification factor over the entire survey area. The solid and dotted curves show the magnification histograms for sources at $z = 4.3$ and $z = 6.8$, respectively.

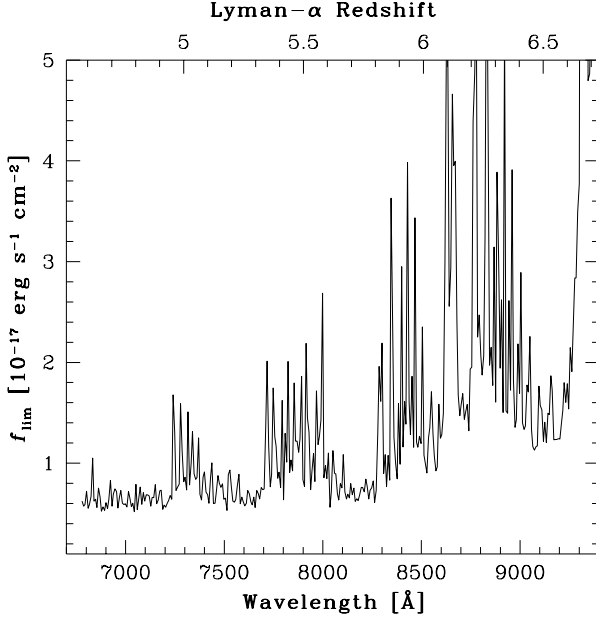


FIG. 8.— Limiting Lyman α flux as a function of wavelength for the survey exposure time of 2000 s, assuming photometric conditions. The curve is the $5\text{-}\sigma$ flux limit to detect an emission line in a $1.3''$ by 7.7 \AA aperture at that wavelength. The top axis is labeled with the redshift corresponding to observed Lyman α falling at the wavelength on the bottom axis. The strong fluctuations in $f_{\text{lim}}(z)$ are caused by atmospheric emission lines, and the rise at high redshift is due to decreased instrumental sensitivity.

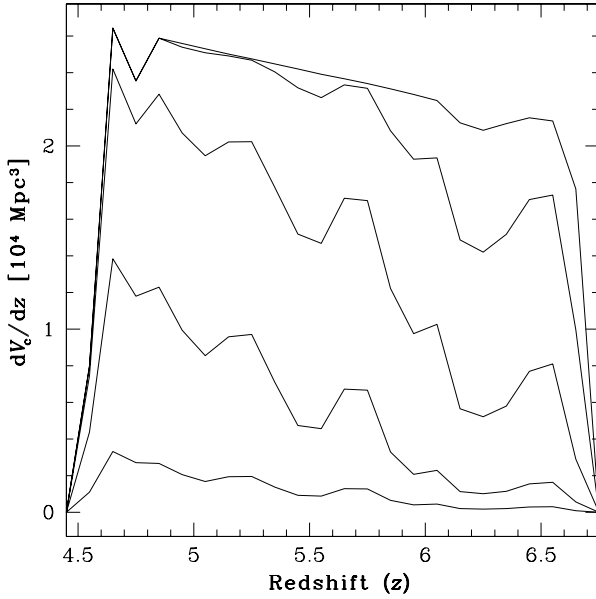


FIG. 9.— The redshift distribution of our survey volume. The curves, from top to bottom, represent the redshift distribution of subsurveys down to limiting luminosity $\log_{10} L = (43.5, 43, 42.5, 42, 41.5)$; for yet lower values of the limiting luminosity, the curves have the shape of the bottom curve, but are scaled down (see Fig. 10).

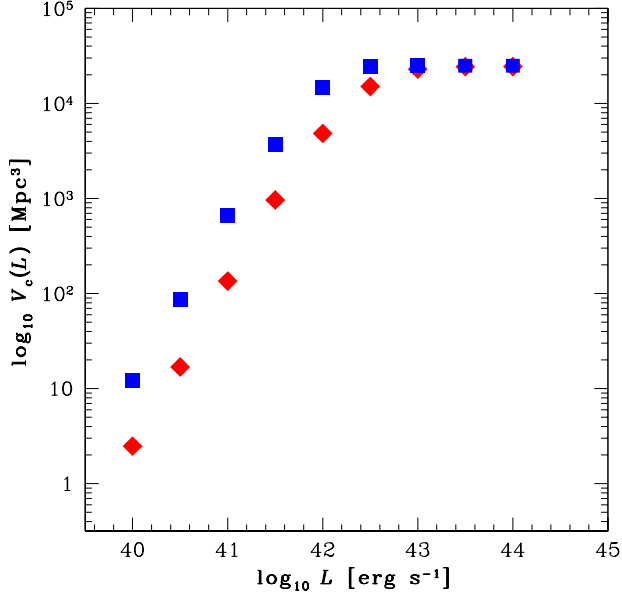


FIG. 10.— Survey volume sensitive to sources with Lyman α line luminosity L . The points show the volume of the survey within which a source of luminosity L would be detected. The survey has been divided into two redshift ranges: the volume with $4.6 < z < 5.6$ is shown with squares, and the volume with $5.6 < z < 6.7$ is shown with diamonds.

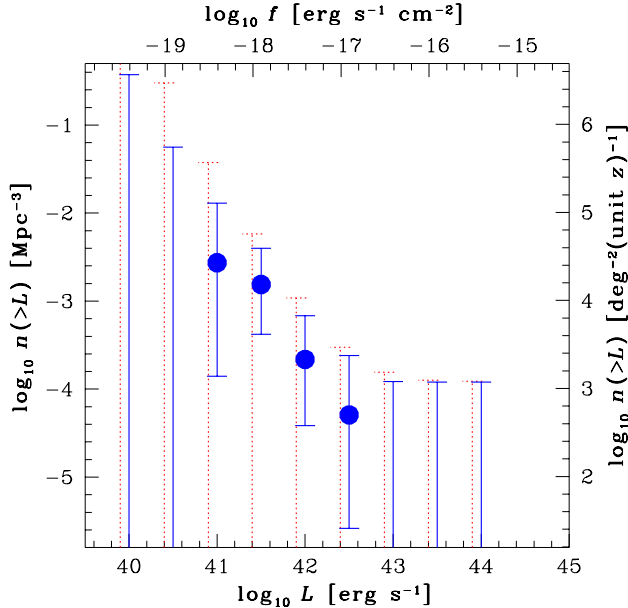


FIG. 11.— Number density of sources brighter than luminosity L , for the three confirmed $z > 4.5$ sources. Each luminosity is treated as an independent sub-survey down to luminosity limit L , and the cumulative number density is calculated from the number of sources in the sub-survey and the volume of the sub-survey. The survey was divided into two redshift bins: the solid lines and points are for $4.6 < z < 5.6$, and the dotted lines (off-set slightly for clarity) are for $5.6 < z < 6.7$. The error bars are 95% limits calculated using Poisson statistics. The top and right axis are labeled in units for comparison of the $4.6 < z < 5.6$ bin results with other work: the left and bottom axes were transformed assuming a redshift of $z = 5.0$.

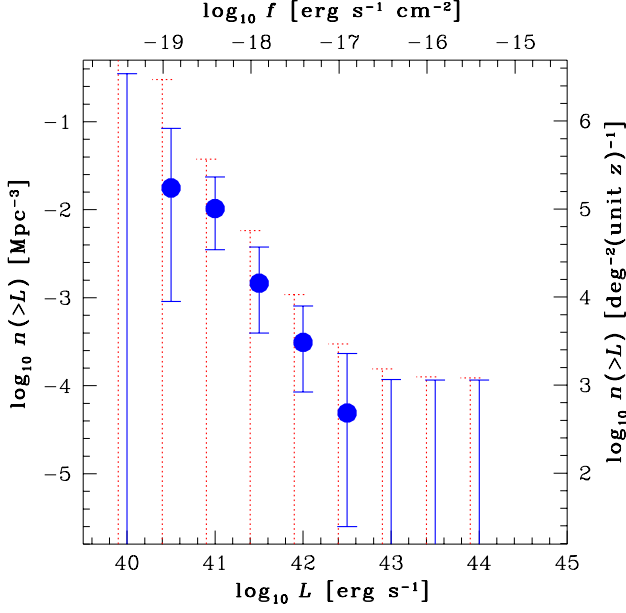


FIG. 12.— Number density of sources brighter than luminosity L , for the three confirmed plus two likely $z > 4.5$ sources. As in Fig. 11.

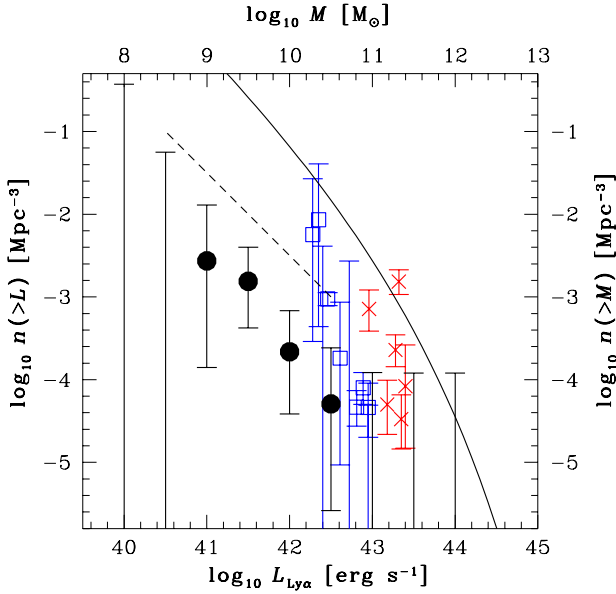


FIG. 13.— Number density of $z \sim 5$ sources brighter than L , for Lyman α surveys and $z \sim 5$ Lyman-break galaxy (LBG) surveys. The solid circles are our cumulative number densities of *confirmed* sources brighter than L for sub-surveys within the $4.6 < z < 5.6$ bin (described in Fig. 11). The open squares are the cumulative number densities of sources brighter than L inferred from other $z \sim 5$ Lyman α line surveys, and the crosses are data from $z \sim 5$ LBG surveys. The LBG surveys were converted to equivalent Lyman α line luminosities (see Section 7.1). The long-dashed curve is a prediction from Haiman & Spaans (1999). The solid curve is the cumulative number density of halos above the mass given on the top axis; the vertical scale is the same. The data are described in Table 3.

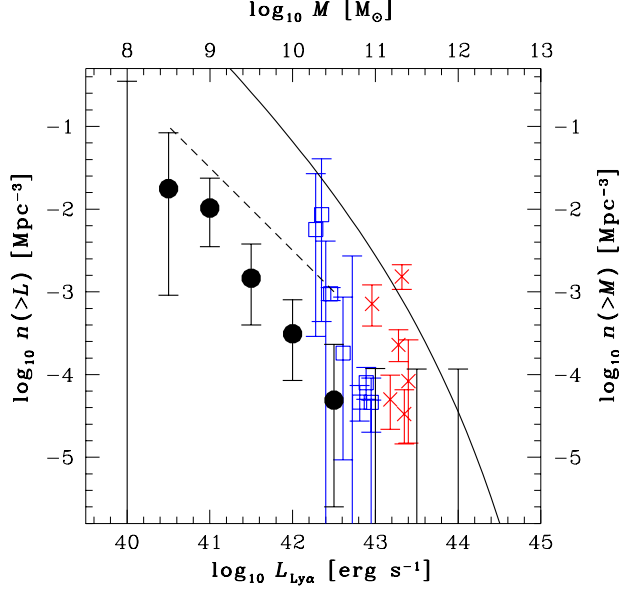


FIG. 14.— Number density of $z \sim 5$ sources brighter than L , for Lyman α surveys and $z \sim 5$ Lyman-break galaxy (LBG) surveys. The solid circles are our cumulative number densities of *confirmed and likely* sources brighter than L for sub-surveys within the $4.6 < z < 5.6$ bin (described in Fig. 12). The other symbols are the same as in Fig. 13.

TABLE 4
GALAXY SURVEYS AT $z \sim 5$

Redshift	$\log_{10} L^a$	Number ^b	Volume ^c	Density ^d	Reference
4.6-5.6	40.5	1(0)	0.0053	$1.8 \times 10^{-2}(0)$	(1)
4.6-5.6	41	4(1)	0.037	$1.1 \times 10^{-2}(2.7 \times 10^{-3})$	(1)
4.6-5.6	41.5	3(3)	0.20	$1.5 \times 10^{-3}(1.5 \times 10^{-3})$	(1)
4.6-5.6	42	3(2)	0.92	$3.3 \times 10^{-2}(2.2 \times 10^{-4})$	(1)
4.6-5.6	42.5	1(1)	2.0	$5.1 \times 10^{-4}(5.1 \times 10^{-4})$	(1)
5-6	42.28	1	0.018	5.6×10^{-3}	(2)
5.7	42.61	1	0.55	1.8×10^{-4}	(3)
6.5	42.95	0	6.1	0	(4)
6.5	42.35	1	0.012	8.5×10^{-3}	(4)
4.9	42.46	87	9.2	9.5×10^{-4}	(5)
5.7	42.81	13	28	4.6×10^{-5}	(6)
6.5	42.89	16	20	8.0×10^{-6}	(7)
5.7	42.95	6	13	4.6×10^{-5}	(8)
5.7	42.72	0	0.11	0	(9)
5.7	42.40	0	0.073	0	(9)
~ 5.8	43.35	6	18	3.3×10^{-5}	(10)
~ 6.3	43.32	26	1.7	1.5×10^{-3}	(11)
~ 5	42.96	10	1.4	7.1×10^{-4}	(12)
~ 5.5	43.40	2	2.4	8.3×10^{-5}	(13)
~ 5.5	43.28	16	7.0	2.3×10^{-3}	(13)
~ 5.3	43.18	6	12	5.0×10^{-5}	(14)

^aSurvey limiting L in units of erg s^{-1}

^bNumber of sources detected in survey

^cVolume of survey in units of 10^4 Mpc^3

^dNumber density of sources, in units of Mpc^{-3}